We are IntechOpen, the world's leading publisher of Open Access books Built by scientists, for scientists

6,900
Open access books available

185,000
International authors and editors

200M
Downloads

Our authors are among the

154
Countries delivered to

TOP 1%
most cited scientists

12.2%
Contributors from top 500 universities



WEB OF SCIENCE™

Selection of our books indexed in the Book Citation Index in Web of Science™ Core Collection (BKCI)

Interested in publishing with us?
Contact book.department@intechopen.com

Numbers displayed above are based on latest data collected.
For more information visit www.intechopen.com



Chapter 4

Application of the Piezoelectricity in an Active and Passive Health Monitoring System

Sébastien Grondel and Christophe Delebarre

Additional information is available at the end of the chapter

http://dx.doi.org/10.5772/54581

1. Introduction

Fibber reinforced composites are nowadays used extensively in aircraft structures because of their properties such as low weight, high stiffness, high strength and fatigue resistance. Nevertheless, they are not exempt from drawbacks, since they are very sensitive to manufacturing processes and service conditions. In particular, their high weakness to low and high velocity impacts has brought new problems for maintenance. These events that are prime sources of delamination and fibber cracking in composite structures are produced either by hazardous conditions (e.g. bird strikes, impacts with foreign objects, etc.) or human errors (tool drops, ground collisions, etc.). In this context, the development of a continuous health monitoring in parallel to the traditional maintenance is a safety issue [1].

Two main strategies are possible to monitor the structural health of composite structures. The first one is the detection of the damaging event continuously, i.e. the detection of the Acoustic Emission (AE) energy that is generally released when the material is bent or cracks due to an external load (pressure, impact, temperature, etc…). This strategy needs permanent monitoring, in flight and on the ground as well [2-4]. The second strategy consists in detecting the damage itself by periodically checking the structural health. Damage detection is then made with help of comparison of the initial state to the actual one. In this situation, the health monitoring system can be either local or global. For the local inspection, the sensor must be in the damaged region, registering permanent strains due to the damage [5-6]. For the global inspection, stimulations are produced in view to induce a structural response, analysed by the sensors. These stimulations can excite the full structure for modal [7] or static analysis [1], or only a small region for the acousto-ultrasonic technique [8-9].

In order to improve the health monitoring system, some scientists have proposed to combine the previously discussed techniques together. Hence, [10] was one of the first to use the same

INTECH
open science | open minds

© 2013 Grondel and Delebarre; licensee InTech. This is an open access article distributed under the terms of the Creative Commons Attribution License (http://creativecommons.org/licenses/by/3.0), which permits unrestricted use, distribution, and reproduction in any medium, provided the original work is properly cited.

piezoelectric transducers in order to perform a passive diagnosis (PSD) and an active sensing diagnosis (ASD). The PSD utilized the sensor measurement to determine the impact force and predict the impact location, whereas the ASD generated diagnostic signals from the actuators to estimate the size of the impact damage. Similarly, [11] demonstrated the possibility to develop an health monitoring system based first on the excitation and reception of guided waves along the structure by using thin piezoelectric transducers (active mode) and secondly on a continuous monitoring taking the same transducers used as AE sensors (passive mode). Their goal was to monitor disbond growth and damaging impact in a composite wingbox structure. To increase the system sensitivity, [12] tried to combine high frequency propagating elastic waves with low-frequency vibrations. This technique also called vibro-ultrasonic technique allows, by applying an additional low frequency, to move the damage, i.e. to open and close crack or delamination. As a result, the high frequency ultrasonic waves are modulated due to varying size of the damage, the intensity of the modulation being proportional to the severity of the damage. [13] proposed the coupling of an electromagnetic sensors network and ceramic piezoelectric sensors. The electromagnetic method is particularly sensitive to local burning, fibber cracking and liquid ingress, whereas the acousto-ultrasonic method is more sensitive to mechanical damage such as delaminations. [14] utilized impedance (local inspection) and guided wave (global inspection) based damage detection techniques simultaneously from surface-mounted piezoelectric transducers to enhance the performance and reliability of damage diagnosis especially under varying temperature conditions. Finally, all these studies demonstrated that the use of complementary techniques tend to extend the detection capability while reducing false alarms.

Despite the extensive literature on the subject, commercial applications of health monitoring systems for damage detection were applied principally to one-dimensional structures such as pipes, and rails, and simple structures like plates. There are two major reasons for this. Firstly, the use of acousto-ultrasonic or acoustic emission techniques in complex structures such as airframes is very complicated due to multiple reflections and mode conversions at features such as ribs and stiffeners which generate signals that are very difficult to interpret. Secondly, many of the proposed methods require a large number of transducers for the monitoring of large structures; this is often not possible or acceptable. Therefore the principal aim of this chapter is to demonstrate the feasibility of using a passive and active system based on few thin piezoelectric transducers to monitor large and complex structures submitted to a series of damaging impacts. The challenge is to detect, analyze and locate damaging impacts with a minimum number of transducers.

2. Experimental procedure

2.1. Structure description

The tests were conducted on a composite wing-box structure (see Figure 1) specially manufactured in order to be representative of an aircraft wing. Hence, wingbox skins were bolted onto a metallic substructure consisting of three metallic spars. The skins used were rectangular

http://dx.doi.org/10.5772/54581

panels (1800*760 mm^2) with a thickness varying from 6 mm to 4 mm and they were made of 913C-HTA composite material. The lay-up and geometry and the material data are given in Appendix A and B, respectively.

Otherwise, as shown in Figure 1(a), the skins had four bonded stringer which were formed around foam cores. Stringer height was 30 mm; width 20 mm and the feet of the stringers were 10 mm wide. The stringers were bonded onto the skins using REDUX 319A structural adhesive.

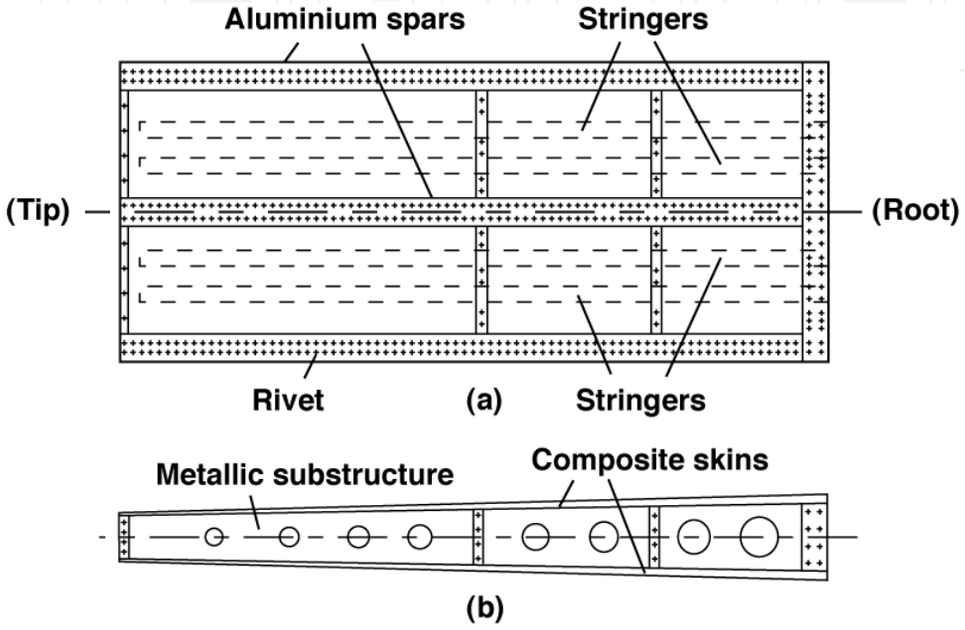


Figure 1. Schematic description of the wing-box structure: (a) Front view; (b) Side view

2.2. Presentation of impact tests

To perform the impacts on the surface of the structure, a mobile tower serving as a guide for the impinger was instrumented with a force sensor. This device thus allowed recording the impact force. In addition, it was possible to apply different energy impacts depending on the height of the fall and the mass of the impinger.

Series of impacts were applied with increasing energy level at three different locations of the structure (see sections 2.3 and 3.4) and after each impact the skin was examined using a manually C-scan ultrasonic system. At the impact location 1, a series of impacts with energy level equal to 6J, 10J, 20J, 30J and 40J was necessary before obtaining a damage of the structure. Using this information, only, two impacts with energy level equal to 6J and 40J were applied at the location 2. Finally, the structure was subjected to successive impacts with energy level equal to 6J, 35J and 40J at the third location.

Figure 2(a) shows the impinger machine while Figures 2(b) and 2(c) illustrate the responses of the force sensor to impacts with energy levels equal to 30J and 40J at location 1. We can notice that the shapes of the force signals are different. Indeed, high frequencies are visible between

2 and 3.5ms on the signal force measured at 40J. The use of the C-Scan described above confirmed that the high frequencies were related to the occurrence of the damage. We will see that this feature can also be used in the analysis of AE signals (see sections 2.5 and 3.2).

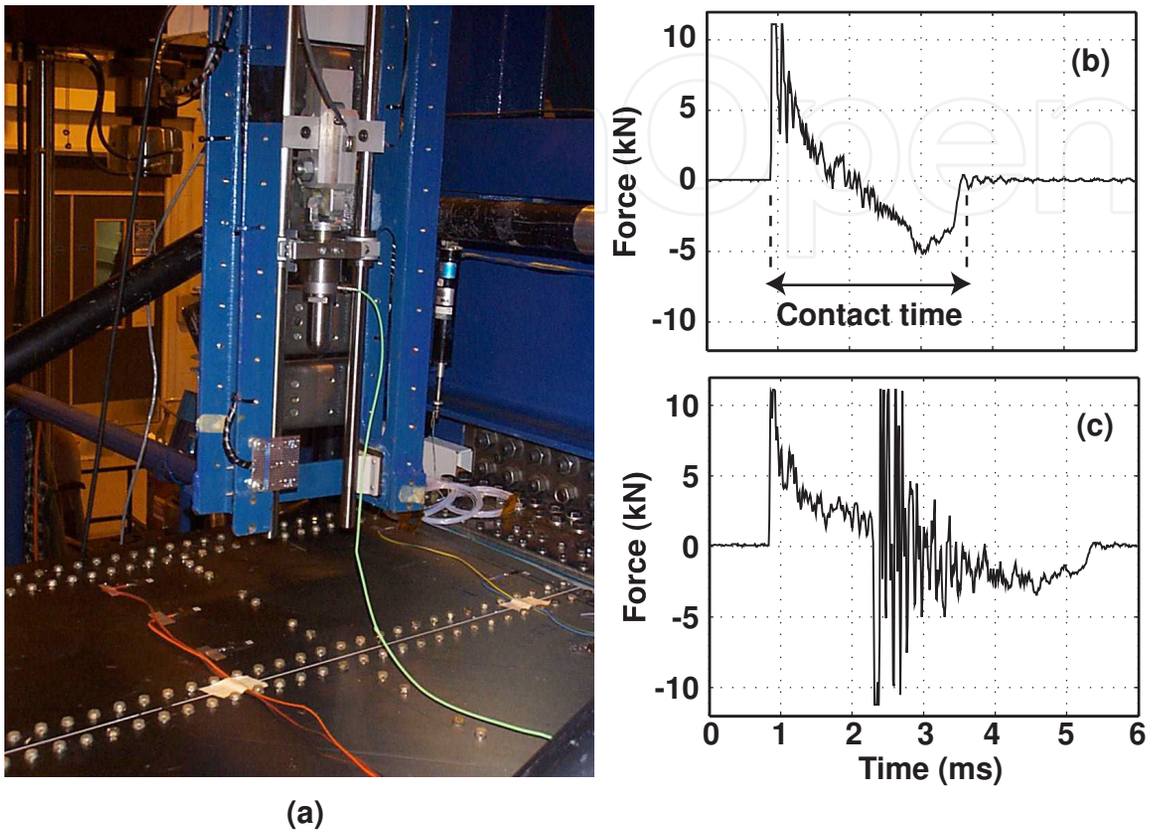


Figure 2. Impinger photography (a), force signal for impact site 1 with energy levels equal to 30J (b) and 40J (c), respectively

2.3. Integration of the health monitoring system

Before the integration of the health monitoring system to the structure, the first task to achieve was to choose an appropriate transducer, i.e. a transducer which could be used complementary to measure either the stress waves generated by damaging impacts (passive mode) or to produce stimulations at discrete time intervals for active health monitoring of the structure (active mode). Since the use of traditional angle probe is not totally fitted because they cannot be permanently fixed on the structure, it was decided to work with low thickness ceramics made of piezoelectric material P1-60 (a standard 'Quartz and Silice' piezoelectric ceramic) and polarized along the thickness. The scaling down of the transducer, particularly the thickness, has the additional advantage of being more adapted to the development of self-monitoring material.

To allow a better directivity of the stimulation in active mode, a rectangular shape for the transducer was privileged. We will see in Section 3.4 that this choice does not affect the results

http://dx.doi.org/10.5772/54581

of damage location in passive mode. Moreover, a general rule [15] of ultrasound emission is to excite the emitting element at its natural resonances rather than at any frequency because this method enables a very efficient conversion from electric to mechanic energy. It also means that special care must be taken to choose the thickness, width and length of the piezoelectric elements. Nevertheless, the height of the piezoelectric elements being chosen small (order of 1 mm), working at the thickness resonance (around 1.8 MHz) is not suitable since it does not correspond to the frequency under study. This also motivated our interest to the transverse resonance. Hence, for application of the stimulation, the dimensions of the transducer have been chosen equal to 1*6*30 mm^3 (see Figure 3(a)), the width resonance corresponding approximately to the frequency of interest according to the properties of the P1-60.

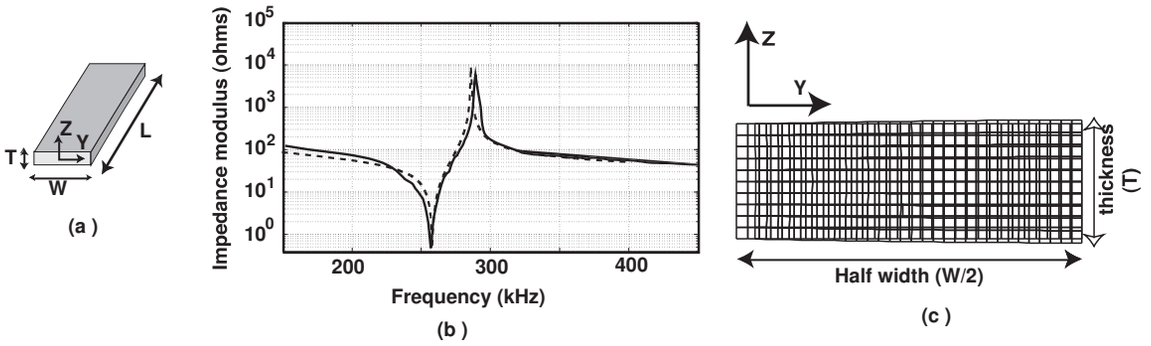


Figure 3. a) Piezoelectric transducer bar, and (b) experimental and computed electrical impedance modulus of the transducer in vacuum, as a function of frequency. Experimental curve: solid line; numerical curve: dashed line. (c) Real part of the displacement field of the piezoelectric transducer under harmonic excitation. (transverse mode at 250 kHz)

In order to confirm this behavior, the impedance of these transducers was measured using a HP 4194A network analyzer and then computed by the finite element method (FEM). Indeed, electrical impedance as a function of frequency is a suitable indicator of resonance modes. Moreover, the computation of the displacements fields by the finite element code enables one to classify these resonance modes.

An illustration of the impedance results in the range 150–450 kHz is presented in Figure 3(b). A very good agreement between the experimental testing and the numerical analysis is observed in this graph. From these curves, one natural vibration mode is clearly visible. Figure 3.c shows the real displacement field of the piezoelectric under excitation at 250 kHz frequency, and it allows one to identify it as a transverse mode. The coupling coefficient of this mode could be determined using the following equation [15]:

$$k_e = \sqrt{1 - \left(f_r / f_a \right)} \tag{1}$$

where f_r and f_a are the resonance and anti-resonance frequencies respectively, of the vibrational mode. This preliminary study, therefore, confirmed the ability to use the transverse resonance

of the transducer to excite ultrasonic waves with a satisfactory electromechanical coupling since k_e was equal to 43%.

Once the transducers selected, the second task dealt with the choice of their location which is extremely important for successful damage detection. Attenuation measurements allowed knowing how far stimulations could be transmitted with a sufficient signal to noise ratio, i.e. more than 30dB. The results showed that for wave propagation parallel to the stringer and a frequency of 250 kHz, which was the working frequency chosen in active mode, stimulations could be propagated for a distance of 80 cm.

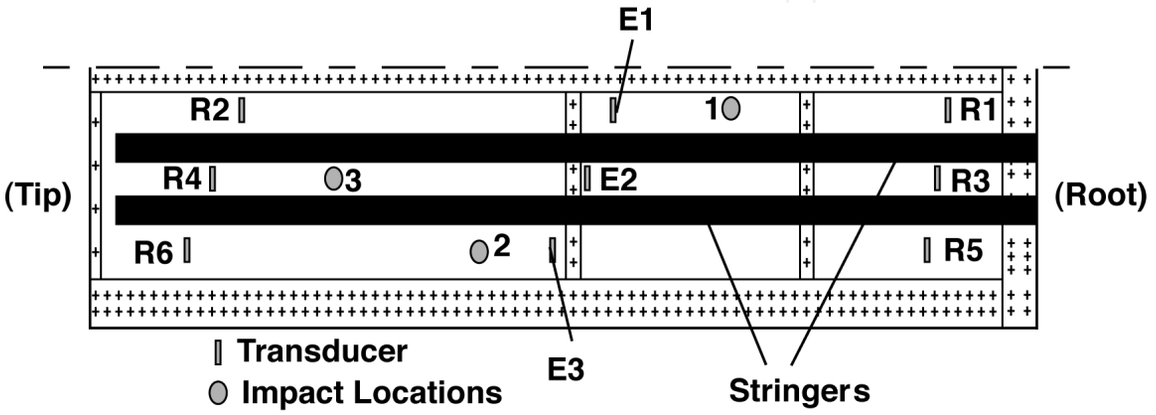


Figure 4. Schematic diagram of the health monitoring set-up –view from underside of the skin

According to these results, nine rectangular piezoelectric elements E_i *(i=1 to 3)* and R_j *(j=1 to 6)* were bonded on the inner surface of the skin as shown in Figure 4. This figure indicates also which of the transducers were used in the actuation *(E)* and which in the sensing *(R)* mode respectively. Moreover, the structure monitoring was divided in six zones using the active and passive system. Generation of a pure single ultrasonic wave between emitters and receivers in active mode was not always possible due to the complexity of the monitored structure as explained in section 2.4, but the integrity of each zone could be monitored. In passive mode, the AE events during each impact were readily detected by the transducers R_j *(j=1 to 6)*.

The equipment used for the instrumentation consisted in two digital oscilloscopes (Lecroy Type LT344) of four channels and three arbitrary calibrated generator functions (HP 33120A). In active mode, the three arbitrary generator functions delivered at discrete time intervals a 250 kHz, 5 –cycle tone burst modified by a Hanning window envelope to the emitters. All the signals from the sensors, i.e. stimulations or AE events were recorded from the digital oscilloscopes and transferred via a GPIB bus to a computer for signal processing.

2.4. Lamb waves system calibration

The laminate nature of fibre reinforced composite materials means that structures can be readily approximated to plate-like structures. As such it can be assumed that AE signals measured in passive mode and stimulations produced in active mode by the piezoelectric transducers will

http://dx.doi.org/10.5772/54581

be propagating as Lamb waves adding a further level of complexity. Lamb waves are elastic perturbations propagating in a solid plate with free boundaries, for which the displacements correspond to various basic propagation modes, with symmetrical and antisymmetrical vibrations. For a given plate thickness *d* and acoustic frequency *f*, there exists a finite number of such propagation modes specified by their phase velocities. A complete description of such propagation characteristics for plates is normally given in the form of a set of dispersion curves, illustrating the plate-mode phase velocity as a function of the frequency–thickness product [16]. Each curve represents a specific normal mode, which is conventionally called A_0, S_0, A_1, S_1, A_2, S_2, etc. A_n denotes antisymmetrical modes and S_n denotes symmetrical ones.

For an optimal use of the active and passive health monitoring system, it was of primary importance to know the characteristics of the Lamb waves that can be propagated in the composite evaluator. In this way, preliminary tests were carried out in order to measure experimentally the velocities of Lamb wave signals as function of the location in the structure and of the frequency. The technique used to perform the analysis of propagating multimode signal was based on a two-dimensional Fourier transform described in [16-17]. Hence, for each thickness variation of the structure, a series of 64 waveforms was recorded along the longitudinal direction with an increment in the position of 1mm. Each Lamb wave response consisted of 1000 samples and the transducers chosen for these tests were the conventional surface mounted transducers (Panametrics A143-SB). The sampling serial of the experiments was 500ns. Before applying the two-dimensional Fourier Transform to the data matrix, 64 zeros and 24 zeros were padded to the end of the signal in both spatial and temporal domains respectively, in order to smooth the results. This method enables to describe the amplitude of Lamb wave signal as function of the frequency and of the wave number.

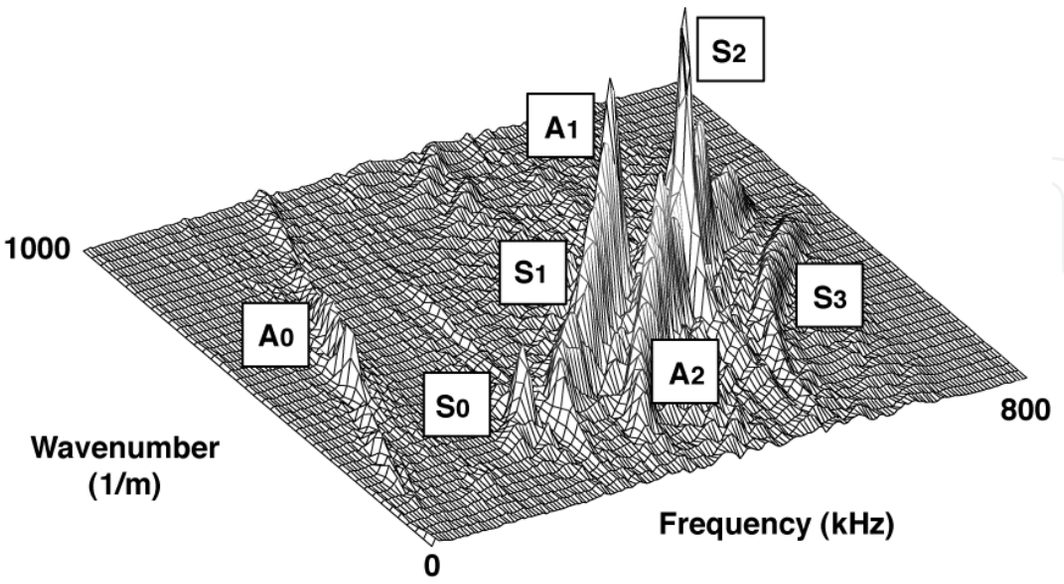


Figure 5. Measurements of the experimental Lamb wave numbers

Figure 5 illustrates an example of the measurements performed from position 800 mm to the position 1400 mm as indicated on Figure 14 in Appendix A. It can be noticed that seven different Lamb modes are propagated between 0 and 800 kHz. In addition, the theoretical phase velocities for three different positions were then computed using the formalism in [18] and compared to the phase velocity experimental measurements deduced from Figure 5. It is shown that the experimental measurements and theoretical results are in good agreement for the first modes (see Figure 6), which is sufficient since the chosen excitation in active mode was 250 kHz and the frequency range of AE events in passive mode did not exceed this value (see section 3.2). This comparative study was performed for each composite plate lay-up leading to satisfactory results.

The computing of the dispersion curves allowed estimating the Lamb modes that could appear in each region for the active mode. Hence, they were only two modes the S_0 and A_0 modes that could exist between the tip and the middle of the panel, while four modes, the S_0, A_0, S_1 and A_1, were expected between the middle and the root of the panel at 250 kHz. Moreover, the amplitudes of the A_0 and A_1 modes, which have wave structures where out-of-plane displacements are dominant at the surface, were relatively small at 250 kHz, because the transducers used in this study were more sensitive to in-plane displacements rather than out-of-plane displacements.

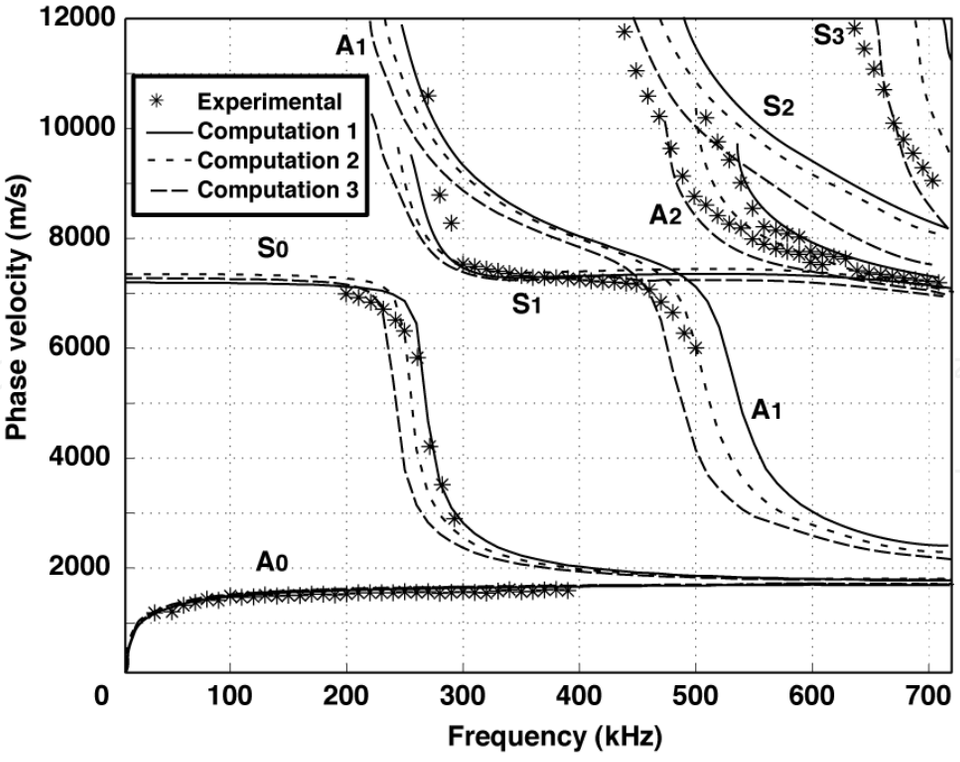


Figure 6. Experimental and theoretical phase velocity determination; Computations 1, 2, 3: thicknesses of 4.5 mm, 4.75 mm and 5 mm respectively

http://dx.doi.org/10.5772/54581

2.5. Damage detection and location procedure

The protocol adopted for the damage detection and location was the following: the proposed health monitoring technique started with the collection of stimulations between each pair of emitter E_i *(i=1 to 3)* and receiver R_j *(j=1 to 6)* for the healthy structure. The series of impacts were then performed at three different locations as indicated on Figure 4 by circles and the AE events were readily detected by the transducers elements R_j *(j=1 to 6)*. After each impact, new collections of stimulations signals were recorded for comparison to the initial ones. As explained in section 2.2, the skin was also examined using the manually C-scan ultrasonic system to provide a rapid assessment of damage state and to allow its severity analysis.

Interpreting the location and severity of damage by using directly time domain signals is often difficult. Consequently, it was decided to implement wavelet transforms for analysing the signals obtained in both passive and active modes and extracting the useful information. In the wavelet analysis, basis functions used were small waves of different scales located at different times of sensor signals that transform the signal to time-frequency scales. Concentration of the signal energy on the time-frequency plane was therefore obtained in terms of amplitude of wavelet coefficient at individual frequency scales.

There are many types of basis wavelet functions such as the Shannon wavelet, Morlet Wavelet, Meyer wavelet, Mexican hat wavelet, Gabor wavelet, etc. Out of these basis wavelet functions, the Gabor wavelet function was adopted in this study since it is known to provide the best time-frequency resolution [19-20]. This wavelet $\psi_g(t)$ is expressed by the following equation :

$$\psi_g(t) = \frac{1}{\sqrt[4]{\pi}}\sqrt{\frac{\omega_0}{\gamma}}e^{-\frac{(\omega_0/\gamma)^2}{2}t^2}e^{i\omega_0 t} \tag{2}$$

and its Fourier transform is :

$$\hat{\psi}_g(\omega) = \frac{\sqrt{2\pi}}{\sqrt[4]{\pi}}\sqrt{\frac{\gamma}{\omega_0}}e^{-\frac{(\gamma/\omega_0)^2}{2}(\omega-\omega_0)^2} \tag{3}$$

where $f_0 = \omega_0/2\pi$ is the central frequency of the Gabor wavelet and $\gamma = \pi\sqrt{2/\ln 2} \approx 5.336$ a shape control parameter. The Gabor function (see eq.2) may be considered as a Gaussian Function centred at $t = 0$ and its Fourier transform (see eq.3) centred at $\omega = \omega_0$. Using the Gabor function as mother wavelet, the continuous wavelet transform (CWT) of an harmonic waveform $u(x,t)$ is defined as [19-20] :

$$WT(a,b) = \frac{1}{\sqrt{a}}\int_{-\infty}^{+\infty} u(x,t)\,\psi_g^*\left(\frac{t-b}{a}\right)dt \tag{4}$$

where the continuous variables *a* and *b* are the scale and translation parameters of the Gabor function respectively, its bandwidth being proportional to *1/a* (see Fig. 7). The function *WT(a,b)* using the Gabor wavelet thus represents the time-frequency component of *u(x,t)* around $t = b$ and $\omega = \omega_0/a$. By setting $\omega_0=2\pi$, we get *1/a* equal to the frequency *f*. The square modulus of the wavelet transform *WT(a,b)* is associated to the energy distribution of the signal and is also referred to as a scalogram. See [21] for the detailed analysis of the Lamb wave signal using wavelet analysis.

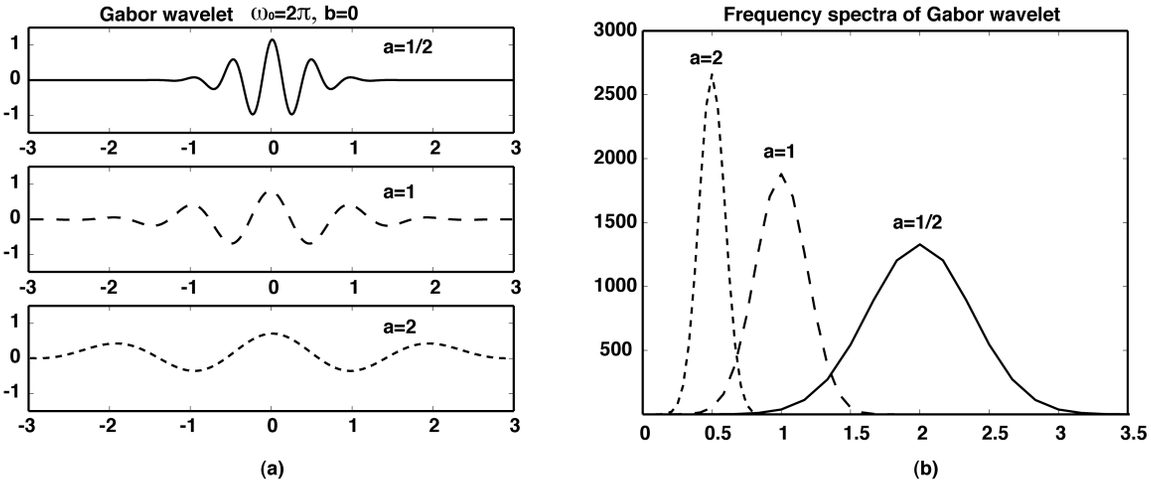


Figure 7. Gabor function at different scales (a) Real part; (b) Modulus Fourier Transform

In order to detect the presence of damage in structure, two kinds of damage sensitive features were deduced from the signals wavelet analysis: a) feature I: maximum value of the received energy in active mode (see Section 3.1) and b) feature II: maximum value of energy of high frequency AE due to damage (see section 3.2) in passive mode. From these features, appropriate damage indexes $DI_A{}^n$ and $DI_p{}^n$ which should reflect changes in the received data due to the damage were proposed as follows:

$$DI_A^n = \left| \frac{\max_{a,b\in R^2}\left(\left|WT_A^0(a,b)\right|^2\right) - \max_{a,b\in R^2}\left(\left|WT_A^n(a,b)\right|^2\right)}{\max_{a,b\in R^2}\left(\left|WT_A^0(a,b)\right|^2\right)} \right| \tag{5}$$

$$DI^n{}_P = \frac{\max_{a\in R,b\in B_2}\left(\left|WT_P^n(a,b)\right|^2\right)}{\max_{a\in R,b\in B_1}\left(\left|WT_P^n(a,b)\right|^2\right)} * \max_{k\in[1\text{to}n]}\left[\frac{\max_{a\in R,b\in B_1}\left(\left|WT_P^k(a,b)\right|^2\right)}{\max_{a\in R,b\in B_2}\left(\left|WT_P^k(a,b)\right|^2\right)}\right] \tag{6}$$

http://dx.doi.org/10.5772/54581

where the superscript n represents the n^{th} impact, N the total number of impacts and the subscripts A and P correspond to the active and passive modes, respectively. The domains B_1 and B_2 refer to the selected time ranges in the time-frequency plane, B_1 corresponds to the duration of the impact whereas B_2 is associated to the duration of the damage AE events (see sections 2.2 and 3.2). WT_P^n are the wavelets coefficients computed from AE signals obtained for each successive n^{th} impact, whereas WT_A^0 and WT_A^n correspond to wavelets coefficients computed from active signals obtained for the healthy structure and after each n^{th} impact, respectively.

Notice that damage indexes DI_A^n and DI_p^n are theoretically equal to zero when no damage is observed. Moreover, threshold values TR_A and TR_P can be obtained from these indexes (see section 3.3). If the damage indexes are larger than the threshold values, damage is detected and its location can be performed. Then, the numbering of damage indexes is reset to zero to allow the detection of damage at other locations.

Locating an AE source or an impact is an inverse problem. If we assume in a first approximation that the group velocity Vg of the AE waves measured from the sensors R_j *(j=1 to 6)* is constant in the structure, the coordinates (x_n, y_n) of the n^{th} impact source can be determined by solving the following set of non-linear equations:

$$(x_{Rj} - x_n)^2 + (y_{Rj} - y_n)^2 - \left[\left(t_m \pm \Delta t_{mj}\right) V_g\right]^2 = 0 \tag{7}$$

Where (x_{Rj}, y_{Rj}) correspond to the coordinates of the j^{th} sensor, t_m is the travel time required to reach the sensor R_m *(m=1 to 6)* and Δt_{mj} are the time differences between sensors R_m and R_j.

For solving this set of non-linear equations with three unknown variables $[x_n, y_n, t_m]$, the method adopted was to combine a Newton's method with an unconstrained optimization in order to ensure the algorithm convergence [22]. Moreover, differences Δt_{mj} in time-frequency wavelet scalograms were used for accurately measuring the arrival time differences.

3. Experimental results and discussion

3.1. Baseline signals in active mode

In active mode, baseline signals were measured for the healthy structure between each pair of emitter E_i *(i=1 to 3)* and receiver R_j *(j=1 to 6)*. Each Lamb wave response consisted of 2000 samples and the sampling frequency was equal to 2MHz. Figure 8 illustrates Lamb wave responses received on the root and on the tip of the panel, respectively. Figure 8(a) shows the Lamb wave response on the transducer R_1 when transducer element E_1 was excited, whereas Figure 8(b) represents the Lamb wave response on the transducer R_6 when transducer element E_3 was excited. In both cases, the energy spectral density of the signal was concentrated around 250 kHz which was the frequency chosen to excite the emitters at their transverse resonance.

From measurements of the time of flights (or arrival times) tS_1 and tS_0 of each mode, the first wave packet of figure 8(a) was identified as the combination of the S_1 and S_0 modes. Since the S_0 mode was excited in a dispersive frequency region, which meant a time spread of the Lamb mode, the amplitude of the S_1 mode was dominant. Similar waveforms were obtained on the root of the panel, i.e. for transducers R_3 and R_5 after excitation of the transducers E_2 and E_3, respectively.

In contrary, while analysing Figure 8(b), it was concluded that the propagated signal corresponded mainly to the propagation of the S_0 mode. Similar waveforms were obtained on the tip of the panel, i.e. for transducers R_2 and R_4, after excitation of the transducers E_1 and E_2, respectively.

In both cases, wavelet analysis was applied in order to estimate the maximum of transmitted energy. The study of the arrival time of the maximum spectral energy density confirmed the identification of the Lamb modes made previously. Measurements performed for the healthy structure and after each impact in active mode will be used in the following to compute the damage index DI_A^n proposed eq.5 and therefore evaluate the sensitivity of these Lamb modes to the damage.

3.2. AE signals preliminary study and processing

Received AE signals for a 6J impact at the location 1 are shown in Figure 9. Each AE signal consisted of 20000 samples and the sampling frequency was equal to 1MHz. Among all received signals, the largest signal arriving earliest in time was that from the sensor R_1 [see figure 9(a)] that was nearest the impact location. As the propagation distances from the impact location to different sensors R_j *(j=1 to 6)* varied significantly, the shapes of the signals recorded by different sensors looked significantly different due to dispersion and attenuation on the stringer.

Since the family of nonlinear equations contained only three unknowns, only three sensors were required to obtain these arrival time differences. Sensor selection was then carried out taking the three first sensors for which the value of amplitude of the time domain signal exceeded a given threshold as shown in Figure 9. It allowed choosing the three sensors with the greatest signal to noise ratio. For that case, sensors R_j *(j=1 to 3)* were selected. Since recording the arrival time differences by the threshold technique directly on the time domain signals did not give accurate results, it was also necessary to use the wavelet scalogram technique for accurately extracting these arrival time differences.

Figure 10 illustrates the procedure for extracting the arrival time differences at the frequency of interest. Firstly, a high pass filter with a cut-off frequency of 15 kHz was applied to all the AE signals in order to privilege the analysis of high frequencies. Indeed, wavelet transform results in better time resolution at higher frequencies. Secondly, the scalogram for each AE signal was performed and represented in contour plot. Thirdly the maximum of the energy spectral density at the frequency of interest was used to estimate the differences of arrival time between the sensors [23]. A preliminary study was therefore done for this first impact of 6J at

http://dx.doi.org/10.5772/54581

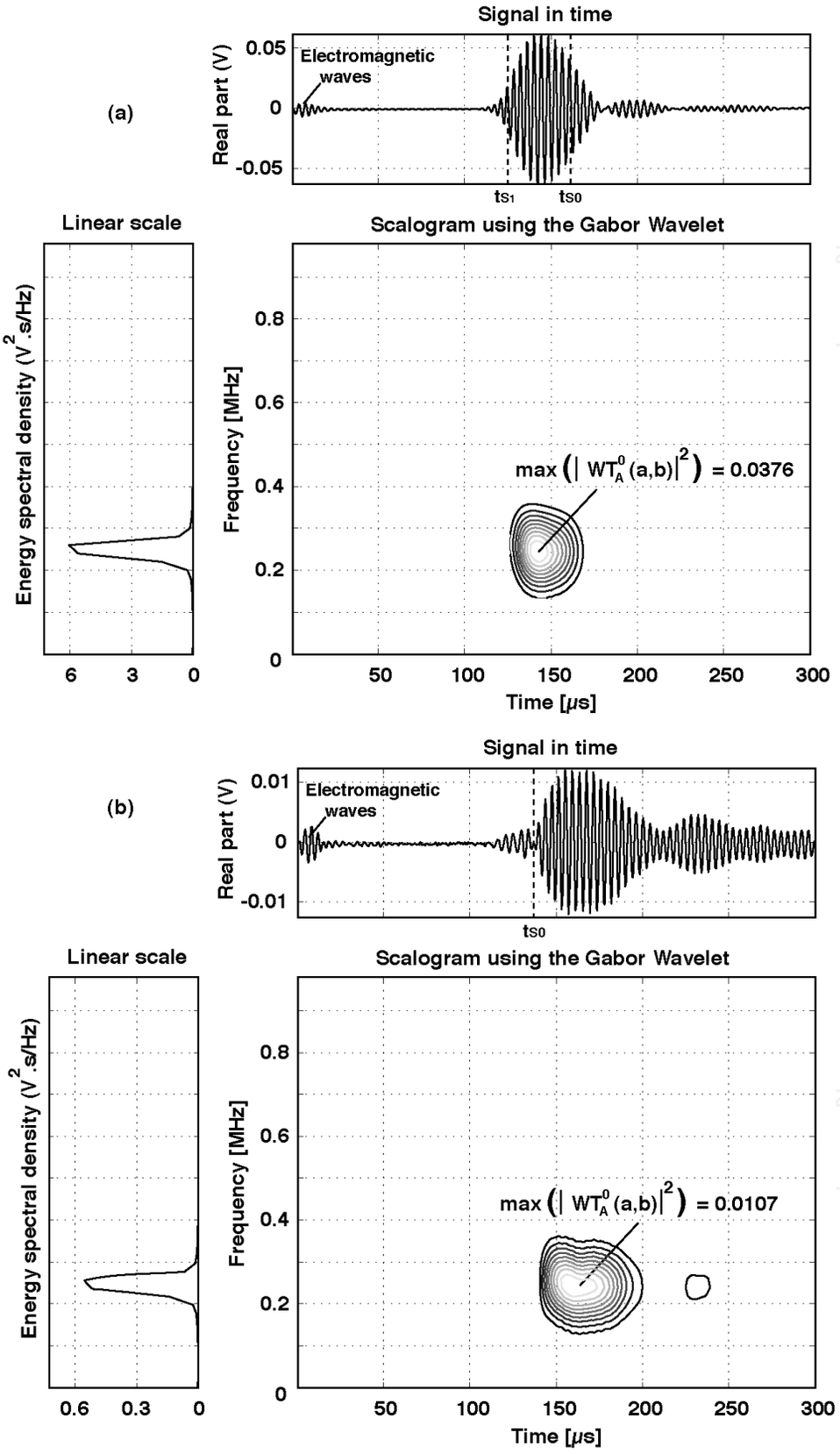


Figure 8. Lamb wave Response and its scalogram (a) at receiver R_1 for the undamaged condition, (b) at receiver R_6 for the undamaged condition

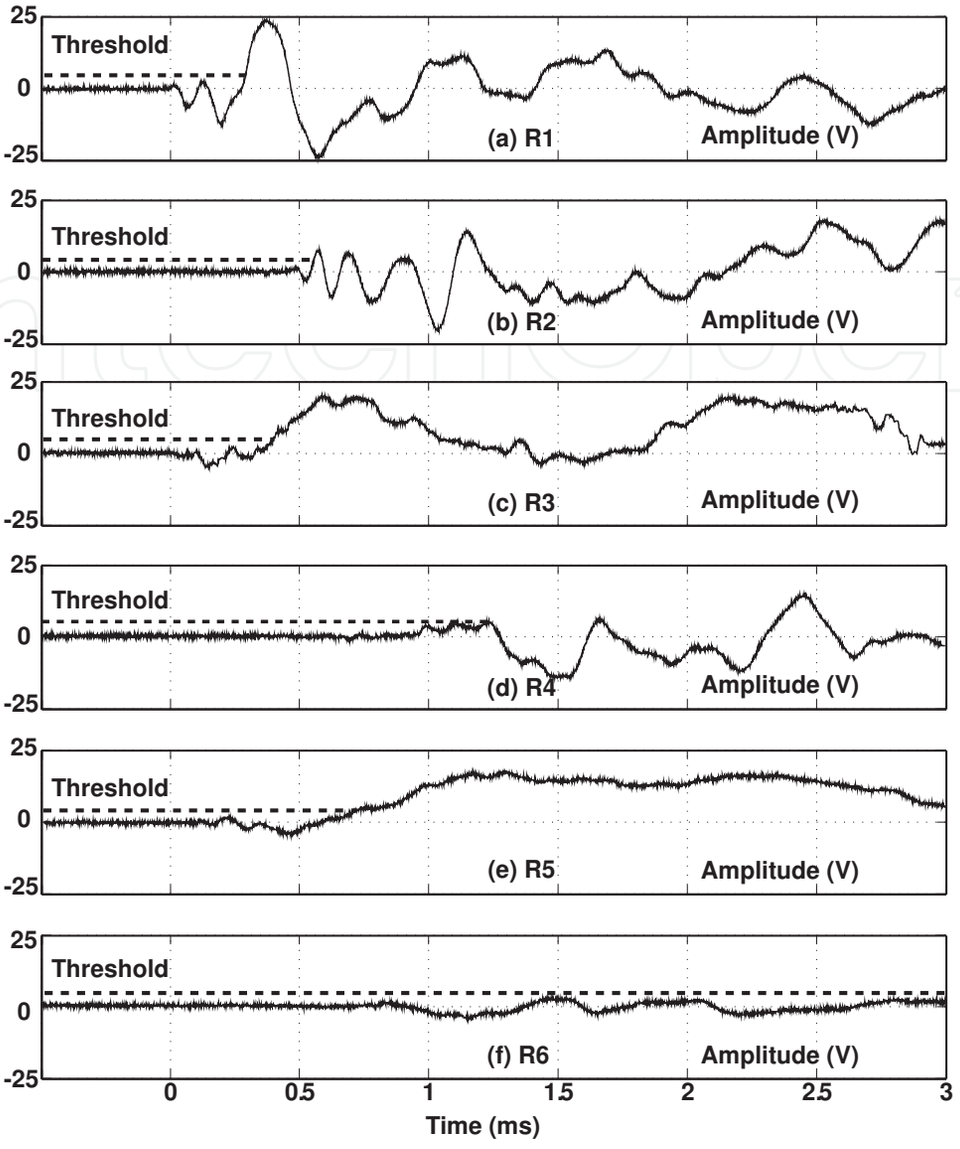


Figure 9. AE data for a 6J-energy impact at location 1 recorded from the sensors :(a) R_1; (b) R_2; (c) R_3; (d) R_4, (e) R_5 and (f) R_6

location 1 to choose the frequency of interest for all the successive impacts and also to estimate the group velocity of the Lamb mode with the dominant energy in the AE signal.

From the plots of Figure 9, it was clear that the exact arrival time of the weak S_0 mode could not be determined since this mode was hidden in the low level noise present in the time history plot. In contrary, the projection (see Figure 10) on the time domain of the ridge around the instantaneous frequency 30 kHz corresponded to the time of arrival of the A_0 mode.

This frequency was chosen since the wavelet analysis showed that the A_0 mode was relatively few dispersive around 30 kHz and was therefore independent from the thickness variation of the structure. Moreover, although signal to noise ratio was higher at lower frequencies, single-velocity arrival times was found to be robust in the presence of electronic noise even for low signal-to-noise ratios. This confirmed the results given in [24].

http://dx.doi.org/10.5772/54581

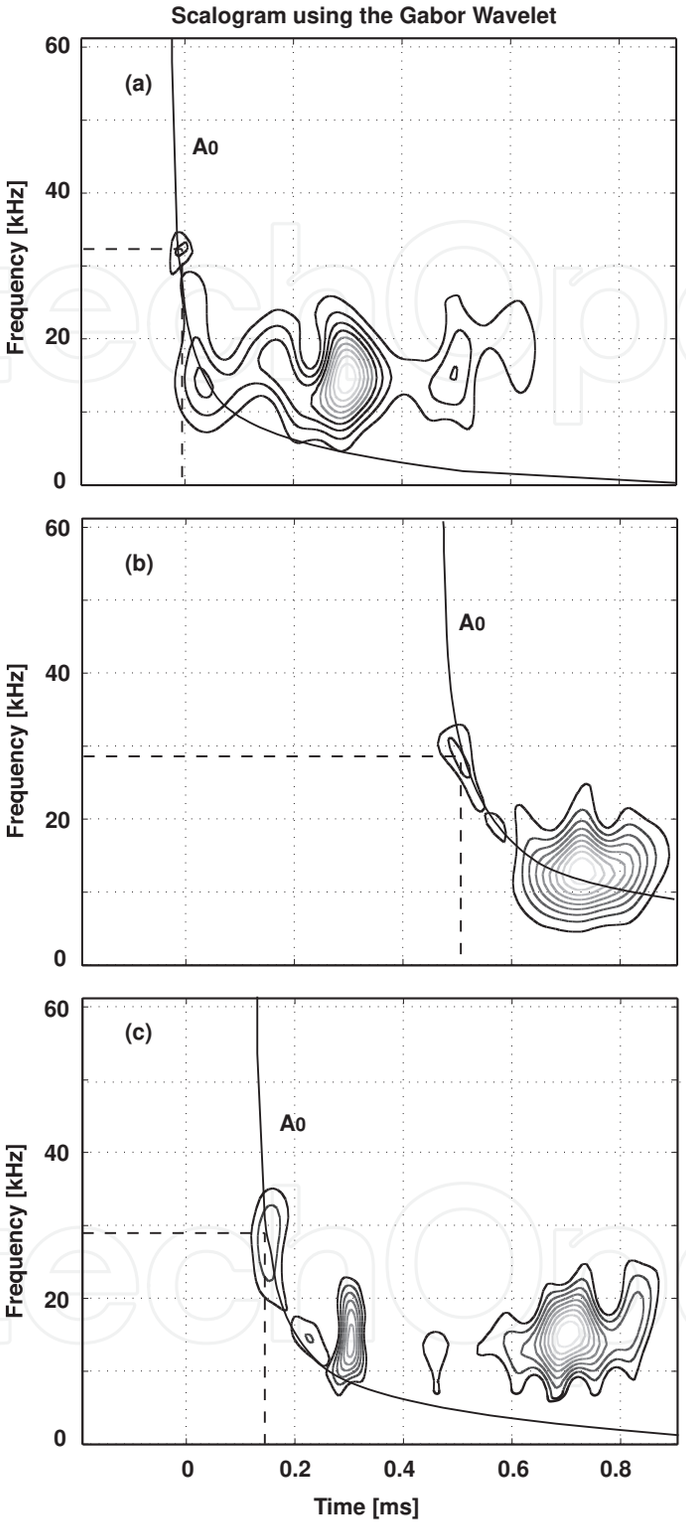


Figure 10. Scalogram of filtered AE data for a 6J-energy impact at location 1 recorded from the sensors :(a) R_1; (b) R_2; (c) R_3

Knowing the location of this first impact a priori, the group velocity was deduced from the difference in arrival time between sensors using eq. 7. The group velocity was equal approx-

imately to 1800m/s, which was in good agreement with the group velocity calculated from the phase velocity measurements of section 2.4. According to the quasi-isotropic nature of the composite plate, the group velocity was considered as constant in all the directions of the plate. Another advantage of using the A_0 mode for this range of frequencies was that the responses of the finite-size sensors converged to that of the point sensors [25] and therefore, the size and shape of the sensors did not influence the measurements.

It was observed during the test that due to severe attenuation of the stringer, the scalogram maxima coefficients in such sensors resulted slightly different. However, the associated frequencies were approximately the same (within a band of 3 kHz) with respect to the nominal value of 30 kHz. This means that the arrival time evaluation error due to frequency shift was negligible.

Figure 11(a) andFigure 11(b) represent the AE signals recorded by the sensor R_1 during impact at location 1 with energy levels equal to 6J and 40J, respectively. After comparison, it could be noticed from the time domain signals that the AE signal recorded for a 40J impact showed the emergence of a second wave packet composed of high frequencies. This result was confirmed using the wavelet analysis, since frequencies until 80 kHz were observed. This meant that the first wave packet corresponded to the impact duration whereas the second wave packet could be related to the damage emergence. This phenomenon already observed on the force sensor (see section 2.2) will be used in the following for the damage index evaluation DI_p^n proposed eq.6. Moreover, this figure allowed estimating the values of the domains *B1* and *B2* denoted in this equation.

3.3. Damage index

In order to facilitate the damage detection and to avoid false alarms, the damage indices defined in eq.5 and eq.6 were calculated and plotted on a two-dimensional damage feature (2-D DF) space. Results for the series of impacts at the three locations are presented in Figures 12(a), 12(b) and 12(c) respectively. For each case, solely the results of the three most sensitive sensors were plotted. A C-scan analysis was therewith proposed for each figure when damage occurred. The amplitude values for these C-scans were represented with an arbitrarily determined colour assignment. According to the "traffic light effect", small indications below the tolerance limit were displayed blue, critical indications were displayed pink, and indications exceeding the tolerance limit were displayed yellow and white.

Considering the results of Figure 12(a), it could be observed first that the damage indexes for non-damaging impact were always lower than the threshold values TR_A =0.2 and TR_P =0.2. On other hand, it could be also noticed that the three sensors R_1, R_2 and R_3 were mostly affected by the impact with energy level of 40J. Indeed, measured values for the passive damage index DI_p were greater than 0.4. As shown in Figure 11(b), these variations corresponded to the emergence in the AE signal of a second wave packet composed of high frequencies when the damage occurred. For this case, the C-scan showed a damage size of approximately 2500 mm^2.

After analyzing the values of active damage index DI_A from Figure 12(a), only the sensor R_1 seemed perturbed since a value greater than 0.5 was measured. From this information, it was

http://dx.doi.org/10.5772/54581

possible to delimit the zone where the damaging impact occurred, i.e. the zone monitored by the emitter E_1 and the receiver R_1 in active mode. Another essential outcome was that this variation of the active damage index revealed a large sensitivity of the Lamb mode S_1 to the damage.

Besides, similar conclusions could be made for the impacts at location 2 (see Figure 12(b)), although only two impacts were performed. In this case, the results demonstrated again a strong sensitivity of the three sensors R_6, R_5 and R_4 to the damaging impact at 40J, as their passive damage indexes DI_p were greater than 0.4. Moreover, a smaller variation of damage index DI_A than in the preceding case was observed for the sensor R_6. This revealed a lower sensitivity of the Lamb mode S_0 than the Lamb mode S_1 to the damage. Finally, results allowed estimating the zone of the damaging impact, i.e. between the emitter E_3 and the receiver R_6.

As expected, similar results were also obtained for the series of impacts at location 3. In fact, the three sensors R_6, R_4 and R_2 demonstrated a great sensitivity to the damaging impact with energy level equal to 40J. Nevertheless, Figure 12(c) enabled also to determine the sensitivity limit of the used health monitoring since a low damaging impact (energy with a level equal to 35J) was tested. For this case, a damage size of 150 mm^2 was measured, but the health monitoring system seemed to be little perturbed, particularly in active mode where the damage index measured DI_A was lower than 0.1. A solution to improve the active system sensitivity would be to work at higher frequencies, but this would require an increase in the number of transducers due to a larger attenuation in the composite at these frequencies.

Taken together, these results demonstrate the feasibility of the proposed health monitoring system to detect damaging impact despite the complexity of the structure. Among the possible ways for improvement of this monitoring and especially to have information also on the severity and characteristic of the damage, one solution would be to develop models in order to better understand the effects of interaction of Lamb modes with damage [26], but also to be able to characterize the sources of damage from acoustic signals [27]. Modeling studies are already proposed for composite structures but very few works are concerned with the case of structures composed of stiffeners [28].

3.4. Damage location

Fig. 13 shows the source location results for all damaging impacts. The real impact positions are plotted with a circle along with the calculated location using the wavelet transform method. Damaging impact locations were estimated each time using the three most sensitive sensors in passive mode (see section 3.2). The data comparisons show good agreement. Table 1 summary these results together with errors. The error was expressed by the following formula :

$$\psi = \sqrt{\left(x_n^r - x_n^c\right)^2 + \left(y_n^r - y_n^c\right)^2} \tag{8}$$

Where (x^r_n, y^r_n) are the coordinates of the real impact position and (x^c_n, y^c_n) the coordinates of the impact location using the algorithm reported in section 2.5. The errors here could be attributed

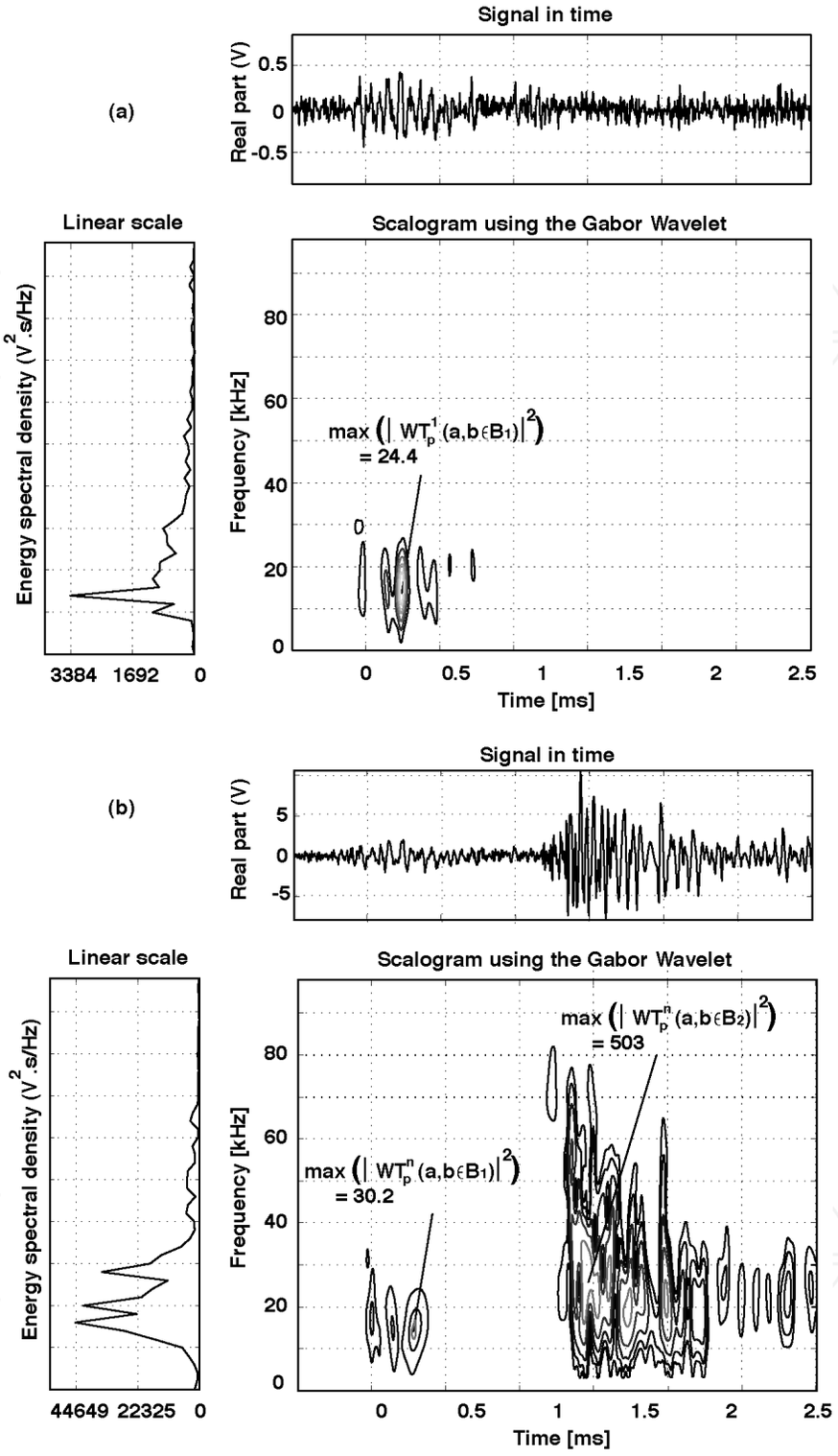


Figure 11. Scalogram of filtered AE data (a) for a 6J and (b) 40J energy impact at location 1 recorded from the sensor R1

to material constants used to calculate the theoretical curves, measurement errors in the placement of sensors and location of the impinger. More likely, this can be due to the presence of the stringers which were not taken into account in the estimation of the group velocity.

http://dx.doi.org/10.5772/54581

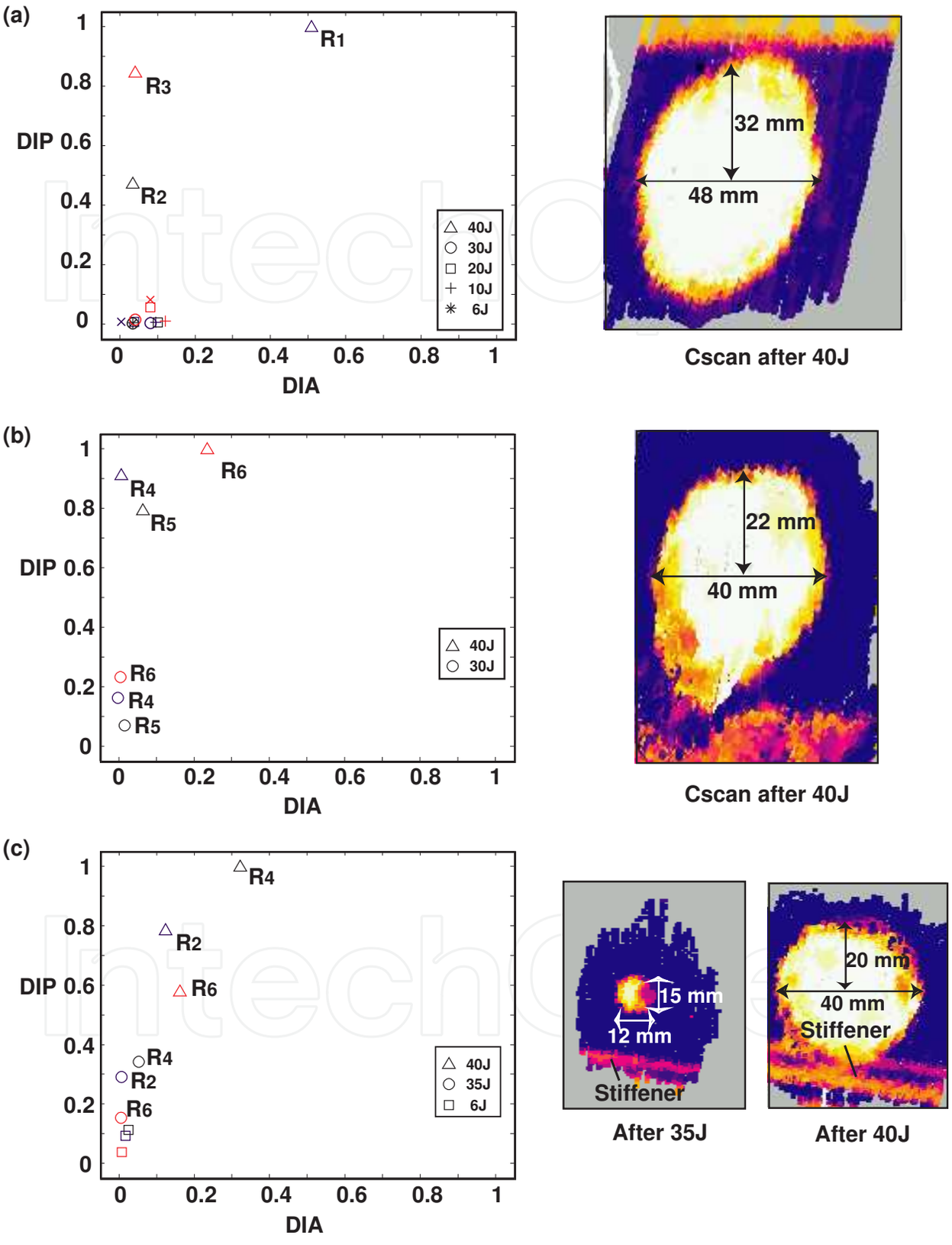


Figure 12. Damage feature space for the series of impacts and the C-scan analysis (a) at location 1, (b) at location 2, (c) at location 3

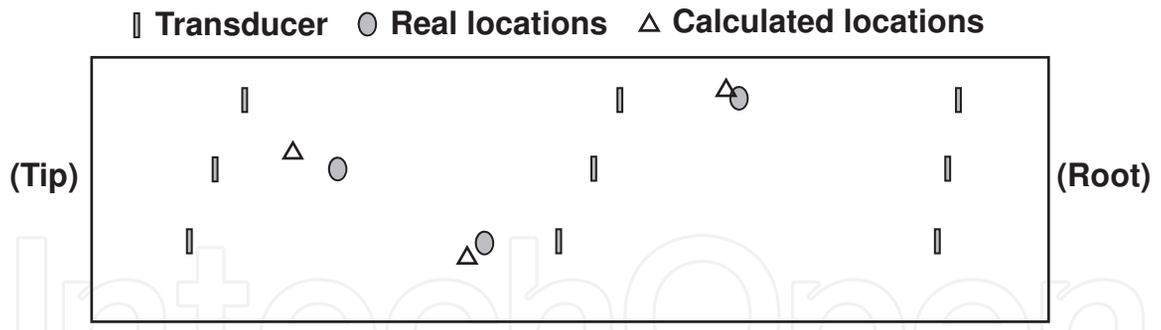


Figure 13. Source location results.

	Impact location 1	Impact location 2	Impact location 3
x-coordinate source location (from algorithm) [mm]	1187	700	375
x-coordinate source location (real value) [mm]	1150	737	462
y-coordinate source location (from algorithm) [mm]	332	95	237
y-coordinate source location (from algorithm) [mm]	314	114	218
Location error [mm]	41	42	89

Table 1. Impacts positions and errors

4. Conclusions

In this paper, experimental investigations were developed to demonstrate the feasibility of using a same piezoelectric Health monitoring system based on both passive and active mode for the inspection of a large and complex structure submitted to impacts. On one hand, the consideration of the AE signatures during impact loadings was of interest as the information retrieved can allowed one to estimate impact location and second to detect a damage occurrence. On the other hand, the experimental results presented here for the active monitoring system revealed also a large sensitivity of the generated Lamb modes to the damage and allowed to confirm the passive diagnostic. Damages indexes were also developed using wavelet analysis and allowed to avoid false alarm, despite the false detection probability could not be measured. Finally, the goal of detecting damaging due to impacts in a complex structure with a minimum of transducers was achieved since only 9 transducers were used for a surface of 1800*380mm^2. More work on the active monitoring and more precisely on the Lamb wave interaction with damage is now required in order to extract the information related to the severity of damage.

http://dx.doi.org/10.5772/54581

Appendix A: Layup and geometry of the structure

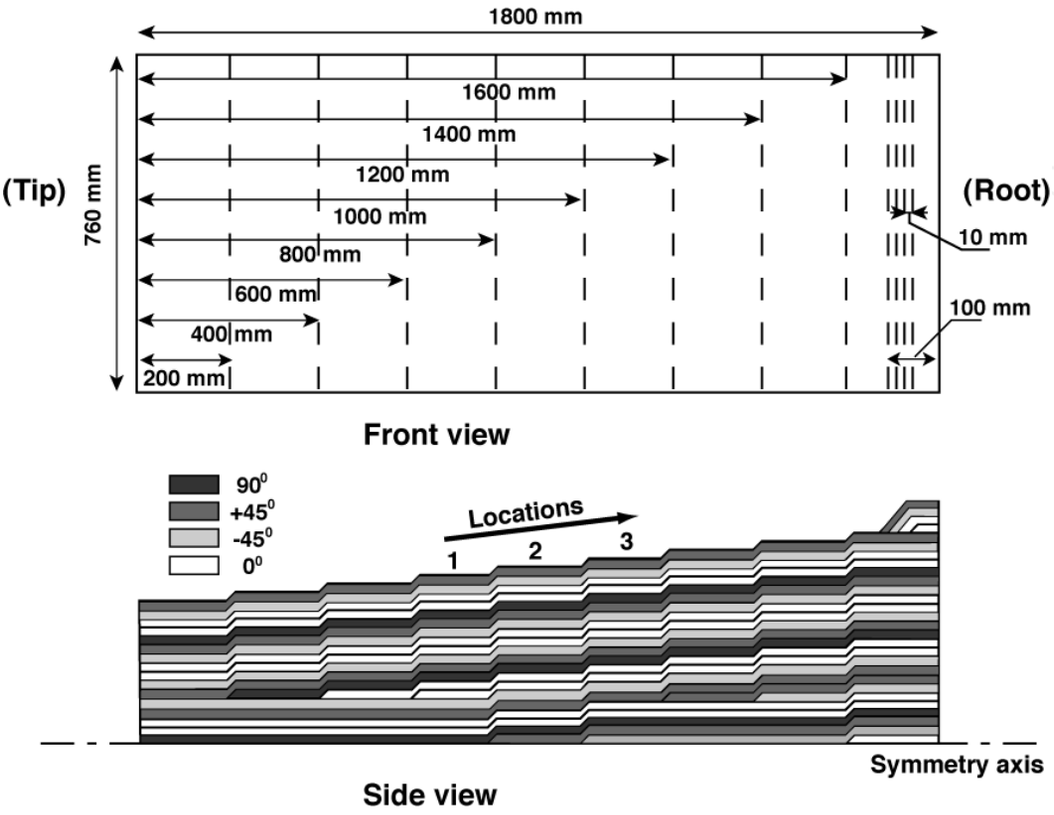


Figure 14. Front and side view of the wing-box structure

Appendix B: Material Data for the 913C-HTA

The skins were made from 913C-HTA material by DSTL (UK). The x_3-axis was defined as the perpendicular axis to the ply-plane.

Nominal ply thickness: 0.125mm, Mass density: 1630kg/m^3, Elastic tensor: E_{11} =158 GPa, E_{22} =E_{33}=9.7 GPa, ν_{12} =ν_{13} =0.3, ν_{23} =0.6, G_{12}=G_{13}=7.4 GPa, G_{23} =3.6 GPa.

Acknowledgements

This work has been performed under the Brite/Euram Monitor (Monitoring On-line Integrated Technologies for Operational Reliability) project no. BE95/1524. The authors acknowledge the support of the Monitor team whose efforts have till date produced successful research. We would also like to thank the C.E.C. who, through their Brite Euram program, has made this research possible.

Author details

Sébastien Grondel* and Christophe Delebarre

*Address all correspondence to: sebastien.grondel@univ-valenciennes.fr

IEMN, Department OAE, IEMN, UMR CNRS 8520, Université de Valenciennes et du Hainaut Cambrésis, Le Mont Houy, Valenciennes, France

References

[1] Staszewsky W. J., Boller C., Tomlinson G., editors. Health monitoring of aerospace Structures – Smart Sensor technologies and Signal processing. Editions John Wiley & Sons; 2004.

[2] Grondel S., Delebarre C., Assaad J., Dupuis J.-P., Reithler L. Fatigue crack monitoring of riveted aluminium strap joints by Lamb wave analysis and acoustic emission measurement techniques. NDT & E International 2002; 35 137-46.

[3] Martin T., Jones A., Read I., Murray S., Haynes D., Lloyd P., Foote P., Noble R., Tunnicliffe D. Structural health monitoring of a carbon fibre structure using low profile piezoelectric, optical and MEMS sensors. Key Engineering Materials 2001; 204-205 371-82.

[4] Eaton M. J., Pullin R., Holford K. M. Acoustic emission source location in composite materials using Delta T Mapping. Composites: Part A 2012; 43 856-863.

[5] Tsutsui H., Kawamata A., Sanda T., Takeda N., Detection of impact damage of stiffened composite panels using embedded small-diameter optical fibers. Smart Mater. Struct. 2004; 13 1284.

[6] Bocherens E., Bourasseau S., Dewynter-Marty V., Berenger H. Damage Detection in a radome sandwich material with embedded fiber optic sensors. Smart. Mater. Struct. 2000; 9 310-315.

[7] Cawley P., Adams R. D. The location of defects in structures from measurements of natural frequencies. Journal of Strain Analysis 1979; 14 49-57.

[8] Grondel S., Paget C. A., Delebarre C., Assaad J. and Levin K. Design of optimal configuration for generating A0 Lamb mode in a composite plate using piezoceramic transducers. J. Acoust. Soc. Am. 2002; 112 84-90.

[9] Paget C. A., Grondel S., Levin K., Delebarre C. Damage assessment in composites by Lamb waves and wavelets coefficients. Smart. Mater. Struct. 2003; 12 393-402.

[10] Choi K., Keilers C. H. Jr, Chang F. K. Impact damage detection in composite structures using distributed piezoceramics. AIAA/ASME/ASCE/AHS/ASC Structures, Structural Dynamics, and Materials Conf. 1994; 1 118-24.

[11] Grondel S., Assaad J., Delebarre C., Moulin E. Health monitoring of a composite wingbox structure. Ultrasonics 2004; 42 819-24.

[12] Staszewski W. J., Buderath M. Vibro-Acousto-Ultrasonics for Fatigue Crack Detection and Monitoring in Aircraft Components. In: Boller C., Staszewski W. (eds.): Proceedings of the 2nd European Workshop on Structural Health Monitoring. DEStech Publication Inc.; 2004.

[13] Lemistre M., Balageas D. A new concept for structural health monitoring applied to composite material. In: Balageas D. (ed.): Proceedings of the first European Workshop on Structural Health Monitoring. DEStech Publication Inc.; 2002.

[14] An Y. -K., Sohn H. Integrated impedance and guided wave based damage detection. Mechanical Systems and Signal Processing 2012; 28 50-62.

[15] Moulin E., Assaad J., Delebarre C. Piezoelectric transducer embedded in a composite plate: application to Lamb wave generation. J. Appl. Phys. 1997; 82 (5) 2049–2055.

[16] Grondel S., Assaad J., Delebarre C., Blanquet P., Moulin E. The propagation of Lamb waves in multi-layered plates: phase velocity measurements. Meas. Sci. Technol. 1999; 10 348.

[17] Alleyne D., Cawley P. A two –dimensional Fourier transform method for the measurement of propagating multimode signals. J. Acoust. Soc. Am. 1991; 89 1159-68.

[18] Nayfeh A. H., Chimenti D. E. The general problem of elastic waves propagation in multilayered anisotropic media. J. Acoust. Soc. Am. 1991; 89 1521-31.

[19] Chui C.K. An introduction to wavelets. Editions San Diego, CA : Academic Press; 1992.

[20] Mallat S.A. Wavelet Tour of Signal Processing. Editions San Diego, CA : Academic Press; 1998.

[21] Jeong H., Jang Y.-S., Wavelet analysis of plate wave propagation in composite laminates. Composite Structures. 2000; 49 443-450.

[22] Dennis J. E., Schnabel R. B. , editors, Numerical Methods for Unconstrained Optimization and Non Linear Equations, editions SIAM; 1996.

[23] Yamada H., Mizutani Y., Nishino H., Takemoto M., Ono K. Lamb Wave Source Location of Impact on Anisotropic Plates. Journal of Acoustic Emission 2000; 18 51-60.

[24] Hamstad H., O' Gallagher A., Gary J. A wavelet transform applied to acoustic emission signals. Journal of Acoustic Emission 2002; 20 62-82.

[25] Di Scalea F. L., Matt H., Bartoli I., Srivastava A., Park G., Farrar C. The fundamental response of piezoelectric guided-wave sensors and applications to damage and im-

pact location. In: Proceedings of the 3rd European Workshop on Structural Health Monitoring. DEStech Publication Inc.; 2006.

[26] Benmeddour F., Grondel S, Assaad J, Moulin E. Study of the fundamental Lamb modes interaction with asymmetrical discontinuities NDT & E International 2008; 41 330-340.

[27] Ben Khalifa W., Jezzine Karim, Grondel S., Lhemery A. Modeling of the Far-Field Acoustic Emission from a Crack Under Stress. In: Proceedings of the 30th European Conference on Acoustic Emission testing and 7th International Conference on Acoustic Emission Granada 2012.

[28] Reusser R.S., D.E. Chimenti, R.A. Roberts, S.D. Holland. Guided plate wave scattering at vertical stiffeners and its effect on source location. Ultrasonics 2012; 52 687–693.

IntechOpen